



From ductile damage to unilateral contact via a point-wise implicit discontinuity

Alireza Daneshyar¹ · Leon Herrmann¹ · Stefan Kollmannsberger¹

Received: 23 June 2023 / Accepted: 30 August 2023 / Published online: 22 September 2023
© The Author(s) 2023

Abstract

Ductile damage models and cohesive laws incorporate the material plasticity entailing the growth of irrecoverable deformations even after complete failure. This unrealistic growth remains concealed until the unilateral effects arising from the crack closure emerge. We address this issue by proposing a new strategy to cope with the entire process of failure, from the very inception in the form of diffuse damage to the final stage, i.e. the emergence of sharp cracks. To this end, we introduce a new strain field, termed *discontinuity strain*, to the conventional additive strain decomposition to account for discontinuities in a continuous sense so that the standard principle of virtual work applies. We treat this strain field similar to a strong discontinuity, yet without introducing new kinematic variables and nonlinear boundary conditions. In this paper, we demonstrate the effectiveness of this new strategy at a simple ductile damage constitutive model. The model uses a scalar damage index to control the degradation process. The discontinuity strain field is injected into the strain decomposition if this damage index exceeds a certain threshold. The threshold corresponds to the limit at which the induced imperfections merge and form a discrete crack. With three-point bending tests under pure mode I and mixed-mode conditions, we demonstrate that this augmentation does not show the early crack closure artifact which is wrongly predicted by plastic damage formulations at load reversal. We also use the concrete damaged plasticity model provided in Abaqus commercial finite element program for our comparison. Lastly, a high-intensity low-cycle fatigue test demonstrates the unilateral effects resulting from the complete closure of the induced crack.

Keywords Implicit discontinuity · Strain decomposition · Unilateral effects

1 Introduction

The last decades have witnessed extensive studies on computational damage and fracture mechanics. With ever growing computational resources at our disposal, various advanced numerical tools representing different aspects of failure problems have emerged, enabling us to predict complex failure scenarios. The complexity arises from the variety of stages involved, comprising the presence of diffuse imperfections, localization of intense deformations, and the formation of distinct sharp cracks. There is a spectrum of options to cope

with the failure process, ranging from purely continuous-based approaches to purely discontinuous ones [1]. On one hand, continuous approaches span the damaged area over a finite width of the medium from the emergence of induced defects, up to the formation of discontinuity surfaces. Therefore, they recast discrete cracks into narrow bands of highly localized deformation with (almost) zero stiffness. Continuum damage models [2–4] and phase-field methods [5–10] belong to this group. On the other hand, discontinuous approaches represent the fracture process zone in the form of displacement jumps, no matter if there truly exists an abrupt change in the displacement field or not. Some prominent methods belonging to this group are the embedded discontinuity model [11–13] and the extended finite element method [14–16].

The origin of continuum damage mechanics can be traced back to the work of Kachanov [17] in which the concept of effective quantities is introduced. Based on that, the material elastoplastic regime is characterized within a fictitious intact configuration at which the mechanical stress is the measure

✉ Alireza Daneshyar
alireza.daneshyar@tum.de

Leon Herrmann
leon.herrmann@tum.de

Stefan Kollmannsberger
stefan.kollmannsberger@tum.de

¹ Chair of Computational Modeling and Simulation, Technical University of Munich, Munich, Germany

of an average force acting on the *undamaged* cross-sectional area of the body. The theory has matured since by extending the idea to cope with the degradation process under different assumptions. Ladevèze [18] introduced the multivariable damage idea to enable simultaneous degradation due to several mechanisms. Tensorial damage variables are introduced in different ways by Leckie and Onat [19], Chaboche [20], and Chow and Wang [21] to consider the non-proportionality of damage on different planes. The unilateral behavior arising from the microdefects closure was also given by Ladevèze and Lemaitre [22] for the isotropic case, and by Desmorat [23] for the anisotropic one. Phase-field models, on the other hand, were originally introduced for interfacial problems, and then tailored for fracture analysis. They were initially introduced for monotonic loading of brittle materials [24]. Then the idea was extended to account for dynamic fracture [25], ductile fracture [26], and fatigue crack growth [27]. The concept behind phase-field fracture models is to compute an auxiliary field identifying the microdefects density whose governing equation is discretized alongside the mechanical problem [28]. Hence, the phase-field fracture theories resemble the gradient-enhanced damage models to some extent.

Early studies under the topic of discontinuous-based approaches rely on linear elastic fracture mechanics within which the plastic zone in front of the crack tip is assumed to be too small to affect the global response [29]. However, this assumption does not hold for most cases especially for those involving crack growth in quasi-brittle and ductile materials. Cohesive zone models resolve this issue by incorporating irreversible phenomena occurring within the fracture process zone through a set of measure zero [30]. They resemble the nonlinear response of the fracture process zone by exerting surface traction on the faces of a fictitious crack that extends beyond the physical crack tip [31]. Hence, cracks must be explicitly defined by means of discontinuity surfaces. Two different strategies can be opted for of which one is to use conforming meshes and the other is to use enriched basis functions. Remeshing is necessary in the former since the crack propagation path is not known in general. This strategy has been employed by Bocca et al. [32] for mixed-mode crack growth in concrete. They used a crack length control scheme to avoid global instability in case of snap-back behavior. Tvergaard and Hutchinson [33] investigate crack growth in elastic–plastic media by introducing a cohesive zone model relying on the work per unit area of crack. Crack growth due to impact damage was investigated by Camacho and Ortiz [34]. They defined cohesive surfaces between each face of adjacent elements. Hence, their model was able to capture fragmentation and crack branching. Tjssens et al. [35] also used the same strategy to enable crack propagation along almost arbitrary directions. They investigated the sensitivity of the results with respect to the mesh align-

ment and tangential cohesive response. Automatic remeshing was the strategy that Bittencourt et al. [36] opted for. They used an interactive crack length control method in conjunction with the cohesive crack approach to simulate arbitrary crack growth. In addition to crack growth simulation, cohesive zone modeling had been employed for other purposes such as delamination analysis by Turon et al. [37], adhesive joint modeling by Campilho et al. [38], joining zones analysis by Töller et al. [39], multiscale modeling by Yang et al. [40], and severe membrane mode deformation analysis by Töller et al. [41], to name a few

The second strategy, i.e. the use of enriched basis functions, is more favorable for problems involving crack growth. This allows the introduction of explicit discontinuities in form of lines or surfaces that do not conform with the element boundaries of the underlying spatial discretization without local remeshing. A prominent variant is the extended finite element method (XFEM). It treats discontinuities by injecting additional degrees of freedom into the finite element spaces undergoing fracture. The method was introduced by Belytschko and Black [42] and Moës et al. [43] in the late '90s and extended to cope with cohesive crack growth by Moës and Belytschko [31] afterward. Employing the same concept, Wells and Sluys [44] enriched the cracked finite elements by adding extra degrees of freedom to represent the displacement jump occurring in the cracking of quasi-brittle materials. Stolarska et al. [45] introduced the level-set approach to the extended finite element method in order to represent the discontinuity faces and also the crack tip. Adding extra enrichment functions to the crack tip elements, Asferg et al. [46] improved the consistency of partially cracked elements by preserving the stress continuity across the fictitious crack. Unger et al. [47] investigated different criteria for the crack growth direction in the context of the extended finite element modeling of cohesive cracks. They used experimental crack growth trajectories to evaluate the results. Zhang and Bu [48] reduced the cost of Newton iterations by presenting new solution procedures that preserve the symmetry of the tangent matrix. Other topics in the context of cohesive zone modeling using the extended finite element method include, but not limited to, composite inelastic modeling by Müller et al. [49], shear band formation by Daneshyar and Mohammadi [50], simulation of fiber-reinforced composites by Pike and Oskay [51], multi-scale modeling of heterogeneous materials by Kästner et al. [52], and biomechanical analysis by Idkaidek et al. [53].

Neither of the aforementioned strategies is self-sufficient in dealing with the entire fracture process. Continuous approaches smear localized band of intense deformation over a finite width of the medium, while discontinuous approaches sample the damaged region on the fictitious crack faces. Both represent the two extreme ends of the spectrum of physical effects well and their strengths and deficiencies

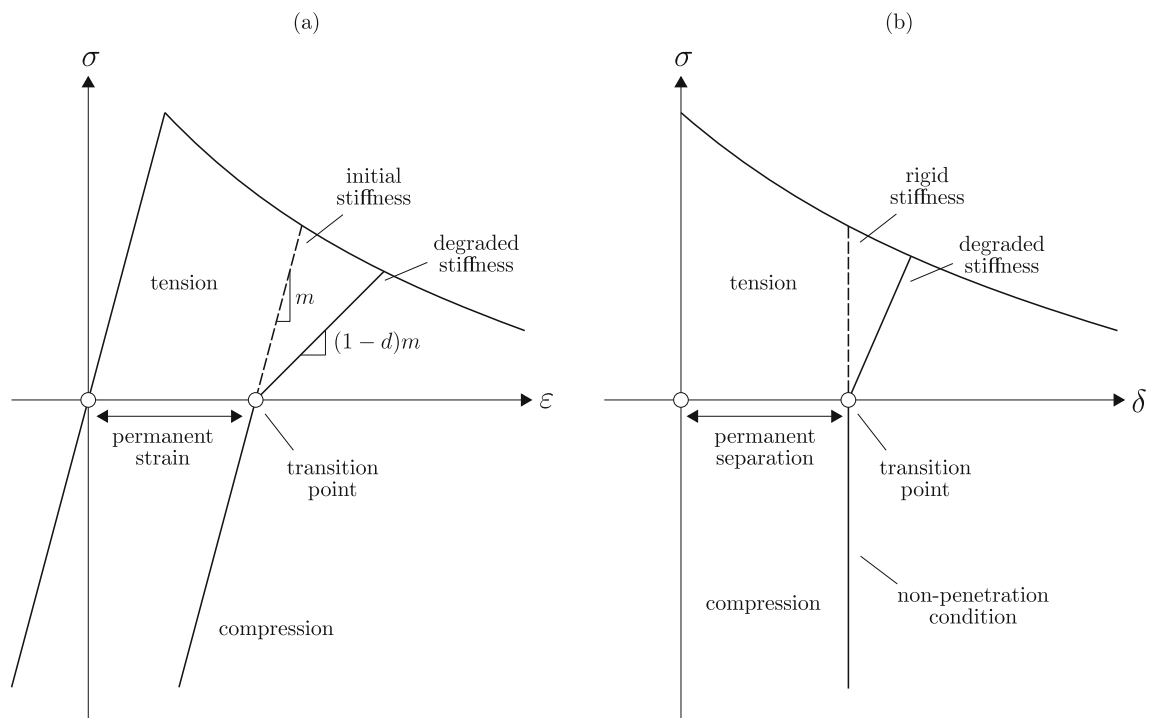


Fig. 1 Generic constitutive laws that incorporate plasticity: **a** continuum damage models, and **b** cohesive models

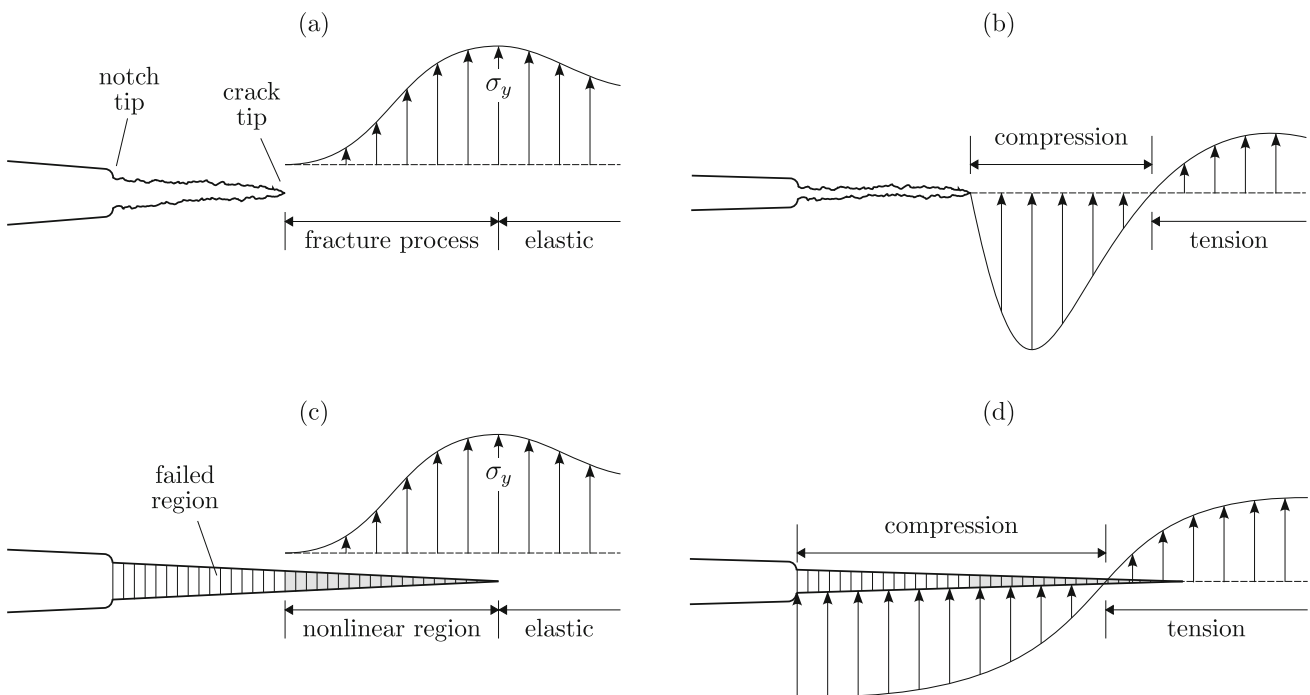


Fig. 2 State of a crack under loaded and relaxed conditions: **a** realistic loaded state, **b** realistic relaxed state, **c** numerical loaded state, and **d** numerical relaxed state

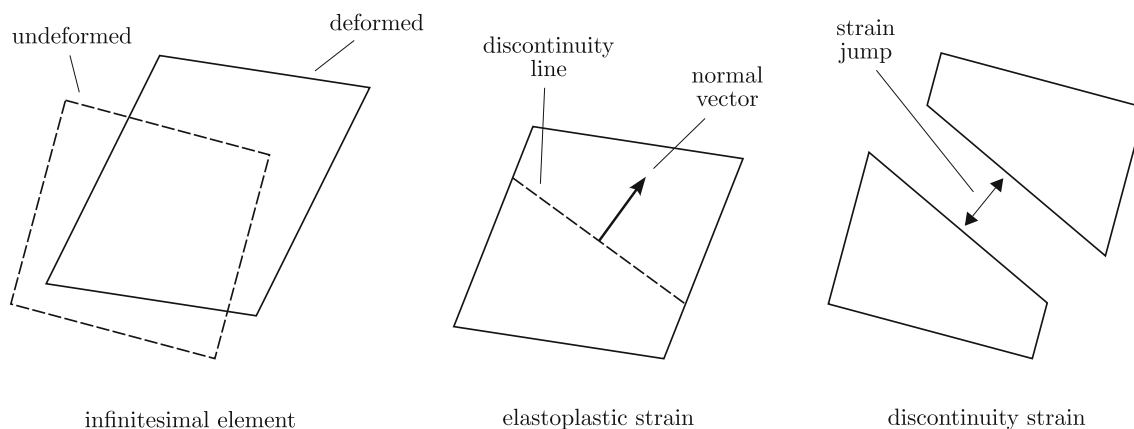
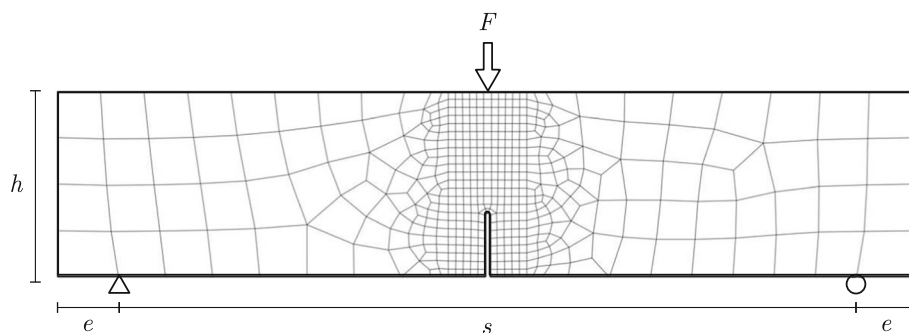


Fig. 3 An abstraction of the additive strain split including the discontinuity strain field

Fig. 4 Geometry, boundary conditions, and finite element mesh of the opening-mode test



complement each other to some extent. Therefore, numerous studies have been devoted to leveraging both approaches by establishing a transition from distributed damage to strong discontinuities. Simone et al. [54] alleviated the unrealistic damage growth resembled by the class of continuous models through combining a regularised continuum framework with a partition of unity finite element method. Introducing the thick level set approach, Moës et al. [55] allowed a straightforward transition from damaged zone to complete fracture once the material is totally damaged. Han et al. [56] proposed a continuous-discontinuous framework considering large deformation kinematics to recast diffuse degraded topologies into sharp crack paths. Dynamic crack propagation induced by gradient-enhanced damage growth was presented by Sun and Löhnert [57]. They coupled transient thermal and dynamic mechanical fields, and used the extended finite element method in three-dimensional settings for representing discrete cracks. Pandey et al. [58] introduced a hybrid methodology by incorporating the extended finite element method and continuum damage mechanics to represent creep-fatigue crack propagation. A continuous-discontinuous strategy within which a thin layer represents the discontinuity emerging due to localized failure is presented by Puccia et al. [59]. This layer behaves similar to the bulk material so that no additional constitutive model associated with cohesive-like approaches is required. Regarding

Table 1 Parameters of the opening-mode test

Parameter	Value	Unit
E	28	GPa
ν	0.2	–
σ_y	3.8	MPa
a	80	–
b	70	–

the conservation of energy during the transition, some continuous-discontinuous approaches inject the discontinuity at the final stage of the fracture process when the material is almost fully degraded to avoid spurious energy release. The combined model of Seabra et al. [60] for damage-driven crack propagation in ductile metals, the fracture-based continuous-discontinuous approach of Sarkar et al. [61], and the enriched continuum model of Negi and Kumar [62] fall into this category. Others use the concept of energy equivalence to define an intermediate state so that the transition can be triggered at any stage in a smooth manner. The hybrid model of Cuvilliez et al. [63], the continuum to discontinuum transition strategy of Roth et al. [64], and the thermodynamically consistent model of Wang and Waisman [65] are some examples of this type.

All of the above and numerous other can accurately address the failure process over moderately complex load-

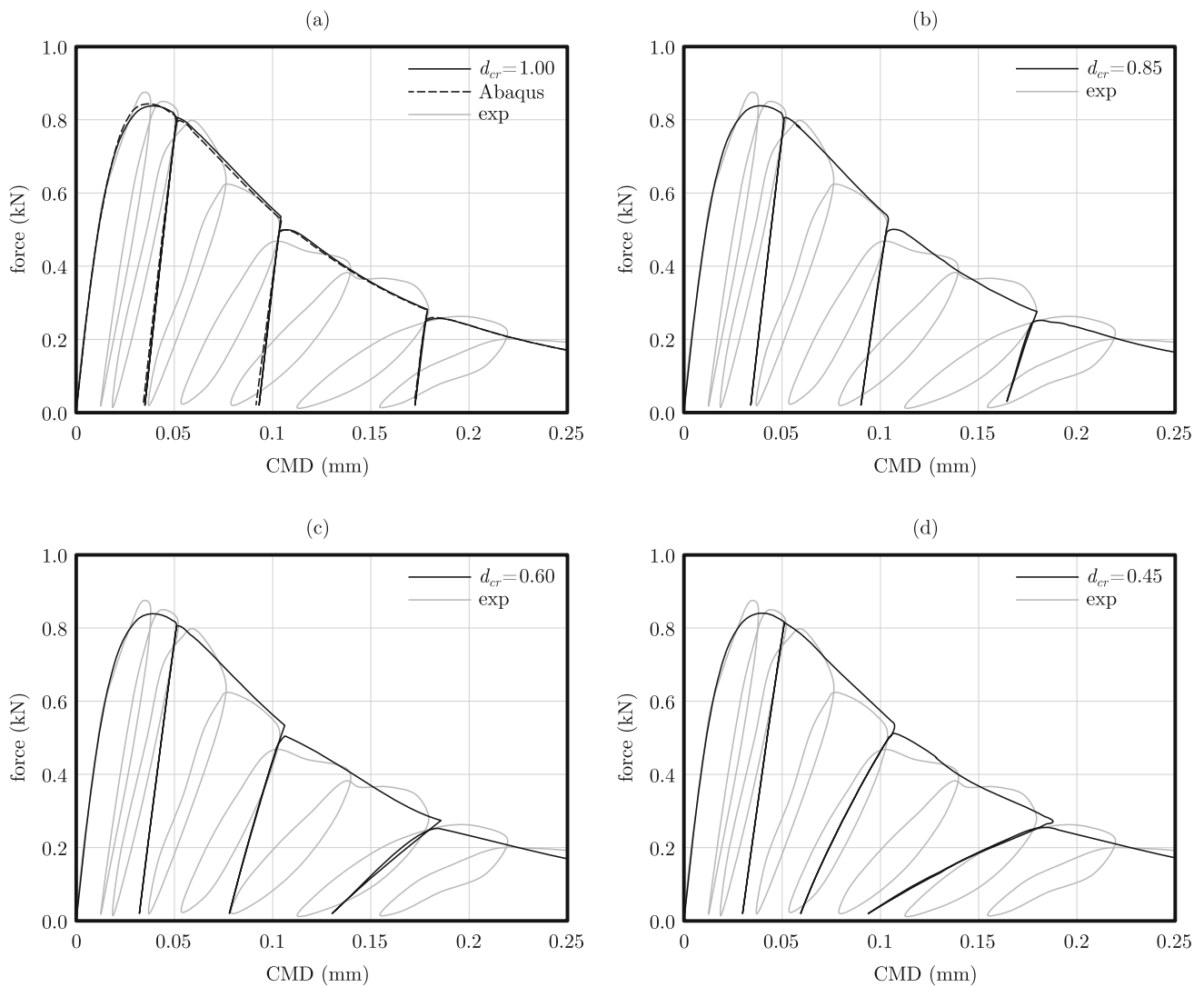


Fig. 5 Comparison of the global responses with the experimental data for the opening-mode test: **a** Abaqus model and $d_{cr} = 1.00$, **b** $d_{cr} = 0.85$, **c** $d_{cr} = 0.60$, and **d** $d_{cr} = 0.45$

ing scenarios. Yet they are not necessarily well-equipped to deal with complex loading paths. The most overlooked aspect of the fracture process in the strategies mentioned is the material response during load reversal. Elegant constitutive models and cohesive laws incorporate plasticity by which irreversible strains and displacement jumps are coupled with reversible ones [66]. As a result, all continuous, discontinuous or hybrid models exhibit excessive unrealistic permanent deformations by construction which are accumulated within the smear or on the discrete fracture process zone. Figure 1 depicts generic constitutive laws of such models. The crack closure effects lead to stiffness recovery upon transition from tension to compression. This unilateral behavior is essential in general loading scenarios, such as cyclic loading [67–70], fatigue tests [71–74], and seismic modeling [75–77], that entail complex strain paths. Obeying the responses shown,

fully degraded regions develop excessive permanent deformations that shift the transition point to the right of the curve. As a result, the unilateral effects may get triggered in a faulty state and lead to artificial stiffening. This is elaborated further in Fig. 2, which shows the normal stress distribution along the crack axis. According to the figure, the fracture process zone nucleated in front of the crack tip spans over the domain that experiences a nonlinear response. As a consequence of balancing the internal forces, part of this zone experiences compressive stresses upon external load removal (see Fig. 2b). However, the crack faces spanning from the notch tip to the crack tips remain traction-free in this relaxed state. This is not the case for the relaxed numerical model as the fully degraded section of the crack develops compressive stresses that affect the global response of the numerical model. This artificial stiffening remains untraced when a con-

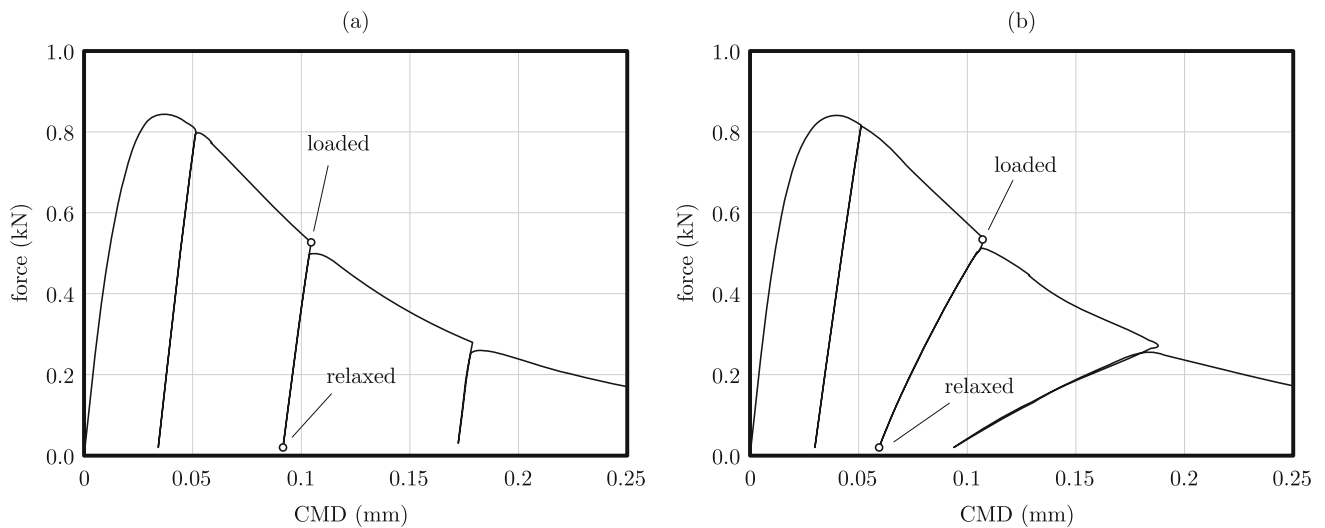


Fig. 6 Loaded and relaxed states at the beginning and the end of the second unloading phase for the opening-mode test: **a** Abaqus model, and **b** $d_{cr} = 0.45$

stantly increasing load is applied and can only be detected in scenarios that involve unloading. A remedy is to limit the growth of permanent deformations to an ultimate state corresponding to the limit at which discrete crack faces emerge. This treatment is completely impractical in the continuous models, yet can be applied in the discontinuous ones by permanently detaching the opposing crack faces and removing the stress continuity condition. In this case, resembling the unilateral effects still invokes the use of computational contact mechanics, which renders the model even more complex.

By contrast, the paper at hand introduces the discontinuity in the strain field to mimic discrete crack faces. As a result, no nonlinear boundary conditions or kinematic variables are involved, preserving the standard form of the virtual work principle. To this end, we organize the body of this text as follows. After this introduction, the additive strain decomposition including the discontinuity strain field is introduced in Sect. 2, followed by the underlying theory of a ductile damage model involving the unilateral effects. It is worth mentioning that a simple damage model is chosen to avoid unnecessary complications arising from the constitutive modeling. However, the discontinuity strain field can be incorporated into other material models regardless of the hypothesis involved. Section 3 is devoted to numerical examples. A three-point bending specimen under pure opening mode is analyzed first. Then, a similar test is conducted under mixed-mode conditions. The complete closure of the crack is also resembled by applying a high-intensity low-cycle load on a double-edge notched specimen before conclusions drawn in Sect. 4 close the paper.

2 Theory

Material inelasticity involves both reversible and non-reversible changes of shape in the consequence of applied loads. The classical models of infinitesimal plasticity characterize these two by means of an additive split with which the total strain is decomposed into an elastic and a plastic part. We augment this additive strain decomposition by introducing the discontinuity strain field $\boldsymbol{\varepsilon}^d$ so that the total strain tensor reads

$$\boldsymbol{\varepsilon} = \boldsymbol{\varepsilon}^e + \boldsymbol{\varepsilon}^p + \boldsymbol{\varepsilon}^d, \quad (1)$$

where $\boldsymbol{\varepsilon}^e$ and $\boldsymbol{\varepsilon}^p$ are the conventional elastic and plastic parts, respectively. Here, the strain field $\boldsymbol{\varepsilon}^d$ represents the induced crack due to the excessive damage growth, but in general, it can mimic any kind of discontinuity. In contrast to the plastic strain $\boldsymbol{\varepsilon}^p$, the discontinuity strain field is reversible, allowing it to resemble the opening and closing of the hypothetical crack. Figure 3 shows an abstraction of this additive decomposition. By activating the discontinuity strain field at a certain damage threshold, which corresponds to the limit of a sharp crack forming due to the complete detachment of material, further plastic straining is prevented. As a consequence, crack closure can occur at this detachment limit in the case of load reversal. Here, we incorporate this strain split in a simple isotropic damage model to keep the constitutive modeling minimal. However, it is worth mentioning once again that the discontinuity strain field can be used in

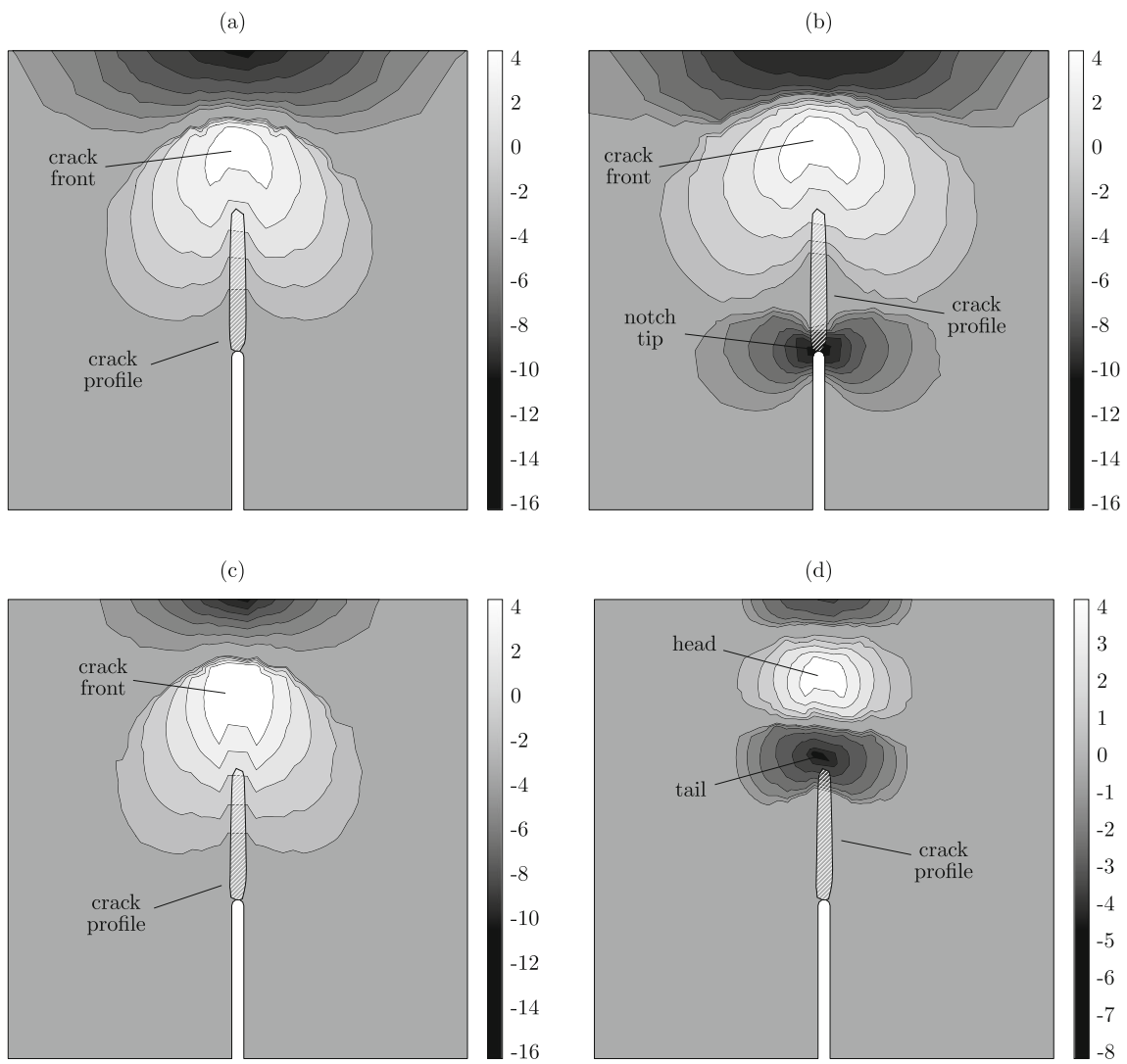


Fig. 7 Stress contours (MPa) at the loaded and relaxed states for the opening-mode test: **a** loaded state in the Abaqus model, **b** relaxed state in the Abaqus model, **c** loaded state in the $d_{cr} = 0.45$ case, and **d** relaxed state in the $d_{cr} = 0.45$ case

Fig. 8 Geometry, boundary conditions, and finite element mesh of the mixed-mode test

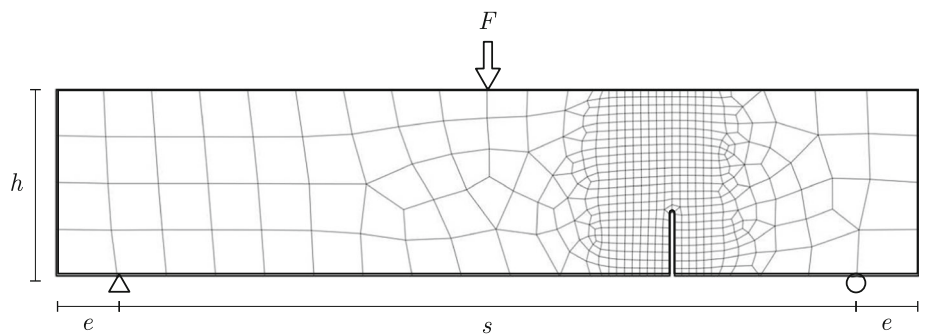


Table 2 Parameters of the mixed-mode test

Parameter	Value	Unit
E	34	GPa
ν	0.2	–
σ_y	4.2	MPa
a	110	–
b	70	–

any material model and also for representing any kind of discontinuity.

Following the concept of effective quantities originally introduced by Kachanov [17], whether the infinitesimal volume element of material is influenced by damage or not, the following general constitutive law of isotropic material applies

$$\tilde{\sigma} = \tilde{\mathbf{D}} : \boldsymbol{\varepsilon}^e, \tag{2}$$

or, equivalently,

$$\tilde{\sigma} = \tilde{\mathbf{D}} : (\boldsymbol{\varepsilon} - \boldsymbol{\varepsilon}^p - \boldsymbol{\varepsilon}^d), \tag{3}$$

where $\tilde{\sigma}$ is the effective stress and $\tilde{\mathbf{D}}$ is the tangent operator of intact material. Note that we preserve this naming convention throughout the text so that the tilde accent refers to the effective configuration.

According to the work of Feenstra and de Borst [78], the yield locus is given in the effective configuration by means of the Rankine maximum principal stress criterion through

$$f(\tilde{\sigma}) = \tilde{\sigma}_{max} - \sigma_y, \tag{4}$$

where σ_y is the yield strength. Hence, the admissibility of the stress state must be preserved by enforcing it to remain inside or on this locus. To this end, the evolution of the plastic strain is given by the associated flow rule

$$\dot{\boldsymbol{\varepsilon}}^p = \dot{\gamma} \partial_{\tilde{\sigma}} f, \tag{5}$$

wherein $\dot{\gamma}$ is a Lagrange multiplier. The pair f and $\dot{\gamma}$ is subjected to the Kuhn–Tucker optimality conditions

$$f \leq 0, \quad \dot{\gamma} \geq 0, \quad \dot{\gamma} f = 0, \tag{6}$$

which enforce the stress state admissibility determining whether yielding occurs or not. Now by defining

$$\boldsymbol{\sigma} = (1 - d)\tilde{\boldsymbol{\sigma}}, \tag{7}$$

the stress tensor in the effective configuration can be mapped to its macroscopically observed counterpart, the Cauchy stress tensor $\boldsymbol{\sigma}$. In the above mapping, the damage index d

represents the density of imperfections reducing the load-bearing area of the infinitesimal volume element of the material. However, in order to establish the unilateral conditions, the above relation must be modified such that the damage index d only applies if the stress state is in tension. To this end, the stress split

$$\tilde{\boldsymbol{\sigma}} = \tilde{\boldsymbol{\sigma}}_t + \tilde{\boldsymbol{\sigma}}_c \tag{8}$$

is defined wherein the subscripts t and c denote the tensile and compressive parts, respectively [79]. The tensile part can be given by [80]

$$\tilde{\boldsymbol{\sigma}}_t = \sum_{i=1}^3 \langle \tilde{\sigma}_i \rangle \mathbf{e}_i \otimes \mathbf{e}_i, \tag{9}$$

wherein

$$\langle x \rangle = \begin{cases} x, & x > 0 \\ 0, & x \leq 0 \end{cases} \tag{10}$$

is the Macaulay bracket, and $\tilde{\sigma}_i$ and \mathbf{e}_i are the i th principal value and principal direction, respectively. Employing the additive split (8), the compressive part reads

$$\tilde{\boldsymbol{\sigma}}_c = \tilde{\boldsymbol{\sigma}} - \sum_{i=1}^3 \langle \tilde{\sigma}_i \rangle \mathbf{e}_i \otimes \mathbf{e}_i. \tag{11}$$

With the tensile and compressive parts at hand, the stress mapping including the unilateral effects is given by

$$\boldsymbol{\sigma} = (1 - d)\tilde{\boldsymbol{\sigma}}_t + \tilde{\boldsymbol{\sigma}}_c. \tag{12}$$

As a result, due to the micro-cracks closure upon transition from tension to compression, the initial stiffness of the material is recovered.

The damage evolution is closely linked to the growth of plastic strain [81]. However, depending on the material being studied, its growth may start as the plastic strain is mobilized or when the yielding process reaches a certain stage. Inspired by the work of Grassl and Jirásek [82], we use the exponential law

$$d = 1 - \exp(-a\bar{\varepsilon}^p), \tag{13}$$

where a is considered as a material constant identifying the magnitude of damage growth, and

$$\bar{\varepsilon}^p = \int_t \dot{\gamma} dt \tag{14}$$

is the accumulated equivalent plastic strain. It is worth mentioning that, for a model aiming at realistic constitutive

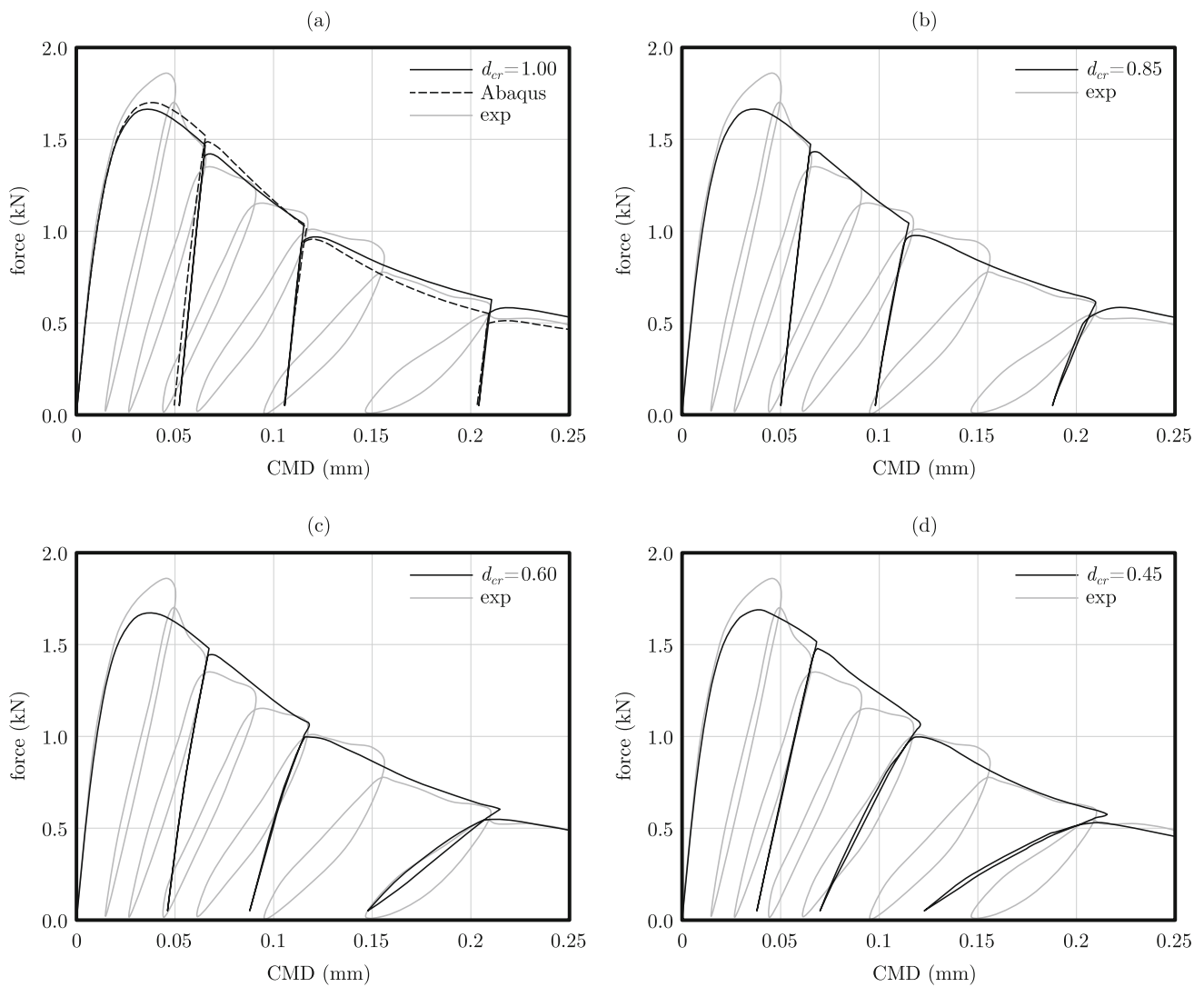


Fig. 9 Comparison of the global responses with the experimental data for the mixed-mode test: **a** Abaqus model and $d_{cr} = 1.00$, **b** $d_{cr} = 0.85$, **c** $d_{cr} = 0.60$, and **d** $d_{cr} = 0.45$

modeling, a more complicated relation can be opted for. Now, at the onset of cracking we have

$$d_{cr} = 1 - \exp(-a\bar{\epsilon}_{cr}^p), \tag{15}$$

where d_{cr} is the critical damage denoting the threshold at which the induced imperfections merge and form a sharp crack. Utilizing the above expression, we can define the critical accumulated equivalent plastic strain at the inception of cracking as

$$\bar{\epsilon}_{cr}^p = -\frac{1}{a} \ln(1 - d_{cr}). \tag{16}$$

Thus, the discontinuity strain field mobilizes if the accumulated equivalent plastic strain reaches the above limit.

Referring to (14), for two arbitrary successive (pseudo-)time steps t and $t + dt$ we have

$$\bar{\epsilon}_{t+dt}^p = \bar{\epsilon}_t^p + \dot{\gamma}. \tag{17}$$

However, the accumulated equivalent plastic strain cannot exceed the limit $\bar{\epsilon}_{cr}^p$. Hence, if the standard return mapping causes an overshoot, there exists an intermediate state between these two successive steps, identified by $t + \alpha dt$, at which

$$\bar{\epsilon}_{t+\alpha dt}^p = \bar{\epsilon}_{cr}^p, \tag{18}$$

and the maximum principal stress hits the yield locus at the same time. Defining λ that denotes the evolution of $\bar{\epsilon}^p$ from the time step t to the time step $t + \alpha dt$, we arrive at

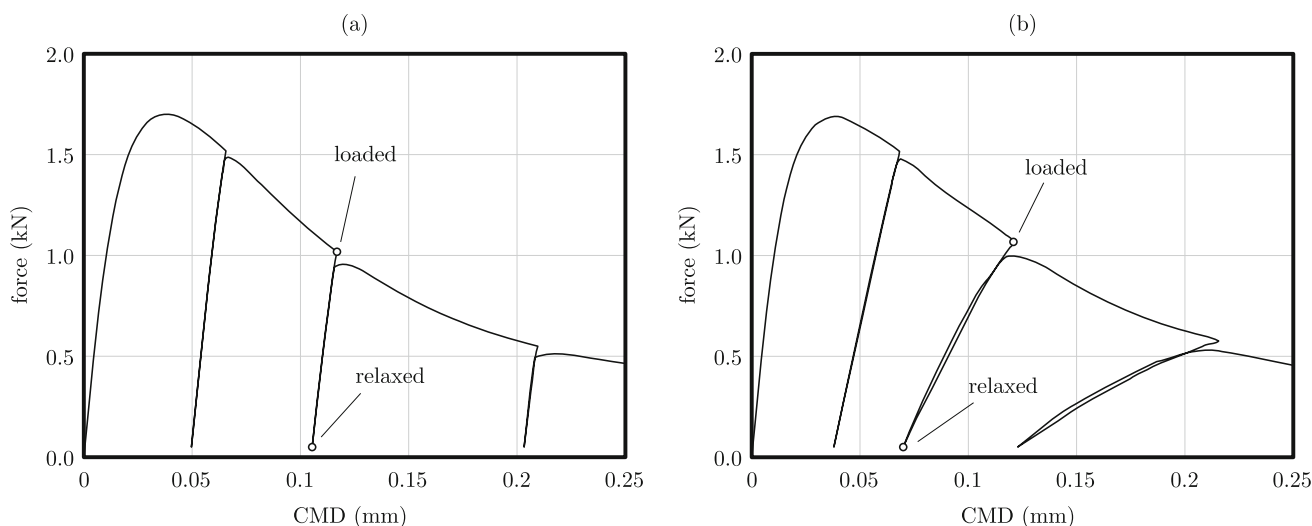


Fig. 10 Loaded and relaxed states at the beginning and the end of the second unloading phase for the mixed-mode test: **a** Abaqus model, and **b** $d_{cr} = 0.45$

$$\bar{\epsilon}_{t+\alpha dt}^P = \bar{\epsilon}_t^P + \lambda. \tag{19}$$

By plugging the magnitude of $\bar{\epsilon}_{t+\alpha dt}^P$ from (18) into the above expression, λ is obtained as

$$\lambda = \bar{\epsilon}_{cr}^P - \bar{\epsilon}_t^P. \tag{20}$$

As a result, the growth of the equivalent plastic strain is known beforehand and the evolution of the plastic strain from t to $t + \alpha dt$ can be given explicitly by

$$\dot{\epsilon}^P = \lambda \partial_{\bar{\sigma}} f. \tag{21}$$

Hence, instead of solving the standard nonlinear return mapping, we must find α such that

$$f(\bar{\sigma}_{t+\alpha dt}) = 0, \tag{22}$$

wherein

$$\bar{\sigma}_{t+\alpha dt} = \bar{\sigma}_t + \tilde{\mathbf{D}} : (\alpha \dot{\epsilon} - \lambda \partial_{\bar{\sigma}} f). \tag{23}$$

From the intermediate state $t + \alpha dt$ onward, further strains are accumulated on the discontinuity strain field. As a result, the discontinuity strain ϵ^d emerges at $t + \alpha dt$ and receives the remaining part of the total strain rate during $t + \alpha dt$ to $t + dt$ so that

$$\epsilon_{t+dt}^d = (1 - \alpha) \dot{\epsilon}. \tag{24}$$

In addition, to comply with the Rankine maximum principal stress criterion, the discontinuity plane is set to the plane of maximum tensile stress at the intermediate state $t + \alpha dt$. The normal vector to this plane, denoted by \mathbf{n} , will be used in the

subsequent stages of the analysis to check whether the crack is open or not. Crack closure is detected if

$$\mathbf{n}^T \epsilon^d \mathbf{n} < 0, \tag{25}$$

meaning that the opposing crack faces penetrate each other. Once again, we must find an intermediate step, denoted by $t + \beta dt$, at which the opposing crack faces meet. By writing the incremental evolution of the discontinuity strain field from t to $t + \beta dt$, we arrive at

$$\epsilon_{t+\beta dt}^d = \epsilon_t^d + \beta \dot{\epsilon}. \tag{26}$$

Solving

$$\mathbf{n}^T \epsilon_t^d \mathbf{n} + \beta \mathbf{n}^T \dot{\epsilon} \mathbf{n} = 0 \tag{27}$$

for β , the exact time of crack closure is obtained. After crack closure, the discontinuity strain field vanishes and the standard elastoplasticity applies until the inception of another crack opening regime. It should be noted that, by employing this formulation, the maximum damage that can be reached is limited to its critical value since no plastic straining occurs afterward. As a result, the degradation process freezes once the damage index reaches its upper limit, which is only acceptable if d_{cr} is chosen extremely close to unity. Otherwise the material preserves its load-bearing capacity and never degrades completely. To allow further damage growth, the exponential function (13) is redefined as

$$d = 1 - \exp(-a\bar{\epsilon}^P) \exp(-b\bar{\epsilon}^c), \tag{28}$$

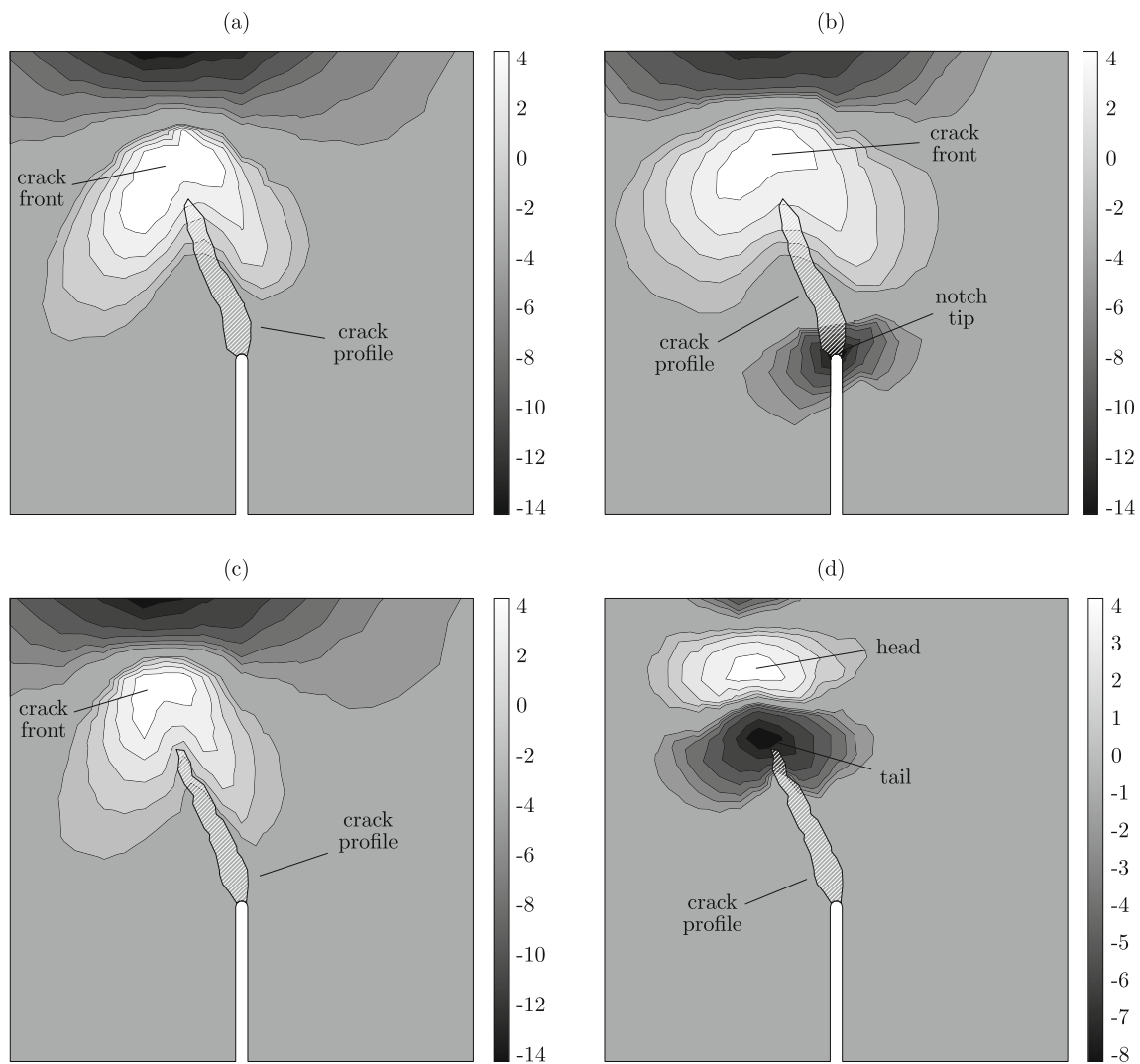


Fig. 11 Stress contours (MPa) at the loaded and relaxed states for the mixed-mode test: **a** loaded state in the Abaqus model, **b** relaxed state in the Abaqus model, **c** loaded state in the $d_{cr} = 0.45$ case, and **d** relaxed state in the $d_{cr} = 0.45$ case

where b is a dimensionless constant used to adjust the damage growth after cracking, and

$$\bar{\varepsilon}^d = \max_{\tau \leq t} (\mathbf{n}^\top \boldsymbol{\varepsilon}^d \mathbf{n}), \tag{29}$$

is the maximum strain jump that is experienced during the loading history. Needless to say that a proper strategy is to establish a relation between the damage growth function (28) and the fracture energy of material so that the constants a and b get linked to a physical property. In addition, it can provide the objectivity of global responses with respect to numerical discretization. However, since this paper is not aimed at the constitutive modeling of material, we will pursue this target in a separate paper in the future.

3 Numerical results

This section is devoted to showing the contribution of the discontinuity strain field in the global responses of specimens undergoing the failure process. To this end, three laboratory tests are chosen, including a pure mode I three-point bending test, a mixed-mode test, and a double-edge notched specimen subjected to cyclic loading. The standard finite element method is used to discretize the domain of problems. Note that the solutions are not unique since the softening response during the failure process induces a local material instability that leads to the ill-posedness of the boundary value problem. This can be cured by injecting a measure of length, known as the material length scale, representing the width of the fracture process zone through non-local or gradient-enhanced formulations or by using the concept of fracture energy equivalence [83]. In the paper at hand, this

Fig. 12 Geometry, boundary conditions, and finite element mesh of the full-cycle test

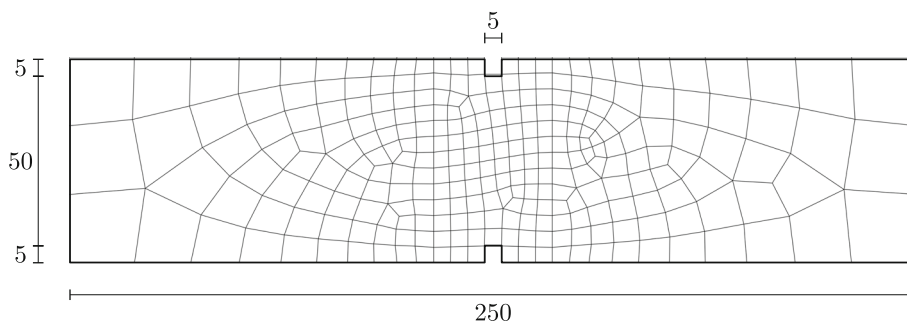


Table 3 Parameters of the full-cycle test

Parameter	Value	Unit
E	25	GPa
ν	0.2	–
σ_y	3.2	MPa
a	150	–
b	140	–

ill-posedness is left untreated to focus only on the introduced discontinuity strain field and keep the message of the paper as clear as possible. As a result, due to the unregularized nature of the field equations, the damage constants a and b are calibrated in accordance with the finite element meshes. This mesh-dependency vanishes once a material length scale is introduced.

We analyze each test using different assumptions of the critical damage d_{cr} to show its effects on the unloading branches. To consider the cases in which the conventional strain decomposition is used, the critical damage d_{cr} is set to unity. As a result, since d is defined by means of an exponential function that never reaches this ultimate value (see the damage growth function in (28)), the discontinuity strain field is simply neglected in the simulations. In addition, to further illustrate the shortcoming of the conventional formulations, the concrete damaged plasticity model of Abaqus finite element program is also used to simulate the tests. This model is capable of reproducing the unilateral effects, which is the key ingredient for revealing the artificial stiffening upon load reversal. Note that one-dimensional stress–strain and damage–strain curves are required to define the post-linear behavior in the Abaqus model. These curves are provided for each example using the calibrated values of E , σ_y , and a in conjunction with the one-dimensional Hooke’s law and the exponential damage growth function in (13). Other parameters of the model are set to their default values.

3.1 Opening-mode test

This numerical example is a replication of the laboratory test of Perdikaris and Romeo [84]. A series of concrete beams

with similar dimensions, yet notched at different offsets were tested. We use the mid-span notched beam for testing the model under a pure mode I loading. Figure 4 shows the finite element model of the beam on the test setup. The dimensions s , h , and e are 304.8, 76.2, and 25.4 mms, respectively. In addition, the notch depth is one-third of the height of the beam. The test is simulated under plane stress conditions with a thickness of 28.6 mms. The material properties of the beam are reported in Table 1. Four cases of d_{cr} are considered, including 1.00, 0.85, 0.60, and 0.45. The former, $d_{cr} = 1.0$, denotes the condition in which the discontinuity strain field is disregarded. Decreasing the value of d_{cr} , the contribution of the discontinuity strain field becomes more pronounced. The test is also modeled by means of the concrete damaged plasticity model of Abaqus.

The global responses of the numerical models are plotted against the experimental data in Fig. 5. The horizontal axis, i.e. the crack mouth displacement (CMD), represents the absolute relative displacement of the crack mouth. Figure 5a clearly shows that the conventional additive strain decomposition, which is the case in the model with $d_{cr} = 1.0$ and the constitutive mode of Abaqus, causes the unloading branches of the curves to have a slope similar to the initial elastic branch. On the other hand, by decreasing the value of d_{cr} , which is accompanied by earlier activation of the discontinuity strain field, the unloading slopes gradually become less steep. The cause of this behavior is elaborated further by comparing the stress distributions before and after the load removal. To this end, consider the loaded and the corresponding relaxed states of the Abaqus model and the $d_{cr} = 0.45$ case depicted in Fig. 6. The stress contours of these cases are shown in Fig. 7. Note that the absolute values of the principal stresses are used so that both tensile and compressive distributions are shown. Figure 7a depicts the stress distributions at the beginning of the unloading phase for the Abaqus model and Fig. 7c for the case of including the discontinuity strain field with the critical damage $d_{cr} = 0.45$. The domain occupied by the fully formed crack is almost stress-free in both cases and the crack front experiences tensile stress with a peak value identical to the yield strength. However, in the relaxed state of the Abaqus model (Fig. 7b), the notch tip experiences a considerable amount of compressive

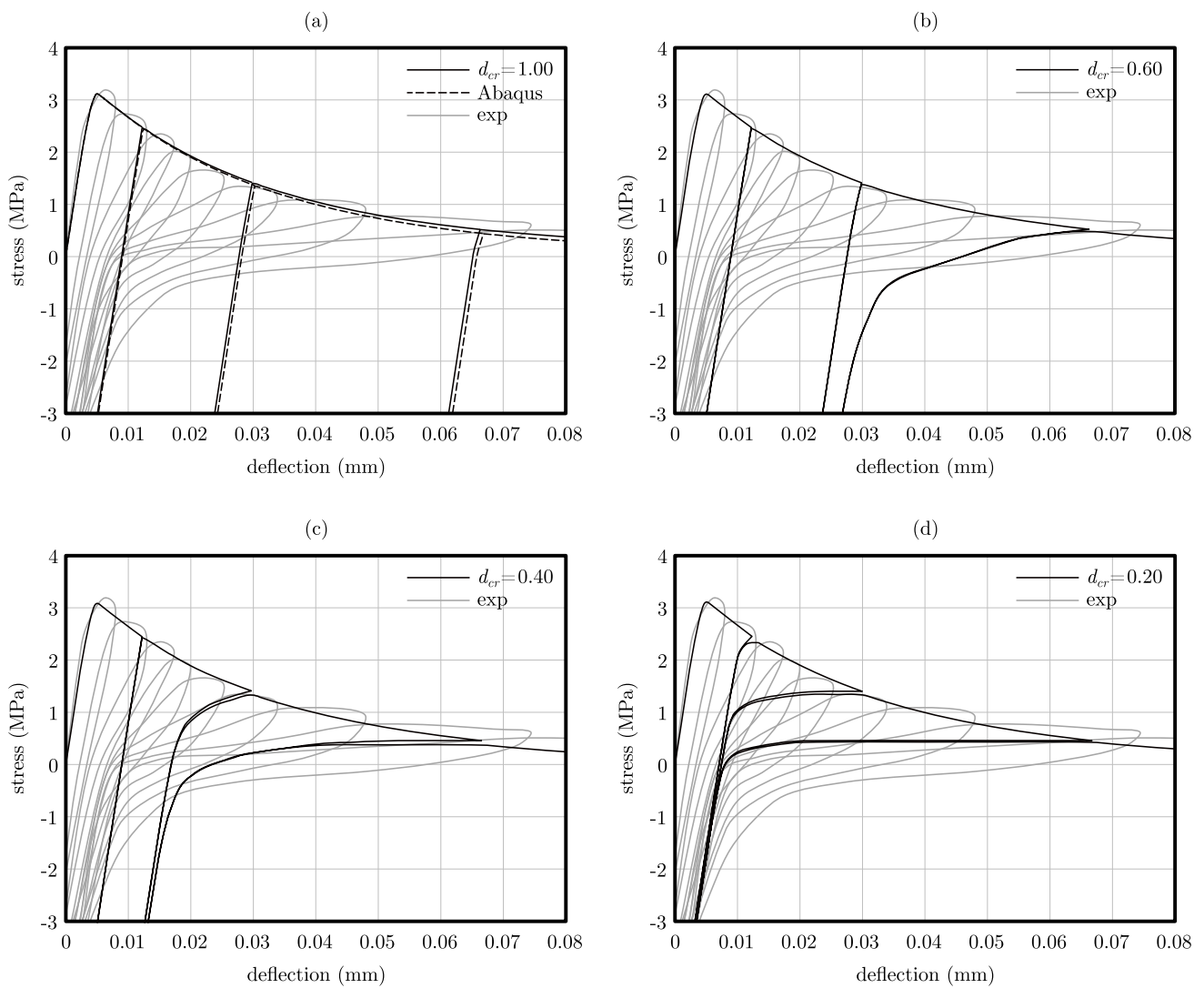


Fig. 13 Comparison of the global responses with the experimental data for the full-cycle test: **a** Abaqus model and $d_{cr} = 1.00$, **b** $d_{cr} = 0.60$, **c** $d_{cr} = 0.40$, and **d** $d_{cr} = 0.20$

sive stress. Hence, a transition from compression to tension exists by moving along the crack axis from the notch tip to the crack front. However, the material must be completely detached and remain stress-free along some part of this axis. This faulty behavior is caused due to the unrealistic growth of plastic strain within the fully degraded regions. This excessive plastic strain causes an early activation of the unilateral effects upon a slight reduction of the total strain, leading to an unrealistically early transition from tension to compression. On the other hand, according to Fig. 7d, by including the discontinuity strain field, some part of the fully damaged region remains stress-free after unloading, and the core of the compressive region is shifted from the notch tip to the middle of the crack. The damaged region located between the tensile and compressive cores can be interpreted as the active fracture process zone, and these two cores indicate the head and tail of this zone. Referring to the schematic stress dis-

tributions shown previously in Fig. 2, we can deduce that by considering the discontinuity strain field, the fully detached section of the crack is reproduced within the model, which is not the case when the discontinuity strain field is not included.

3.2 Mixed-mode test

The second example is also selected from the work of Perdikaris and Romeo. The test setup is similar to the previous one, with the exception that the notch is offset by 75.6 mm from the mid-span (see Fig. 8). The properties presented in Table 2 are used for the numerical model. Similar to the previous test, in addition to the Abaqus model, four cases of $d_{cr} = 1.00$, $d_{cr} = 0.85$, $d_{cr} = 0.60$, and $d_{cr} = 0.45$ are considered.

The applied force versus the crack mouth displacement curves, plotted on the experimental data in Fig. 9, conspicu-

ously demonstrate the contribution of the discontinuity strain field. Referring to the stages marked in Fig. 10 for the Abaqus model and the $d_{cr} = 0.45$ case, a deduction similar to that of the previous test regarding the stress contours shown in Fig. 11 can be drawn. Upon the external load removal, the fully degraded part of the crack develops compressive stress in the Abaqus model, while this part remains stress-free in the $d_{cr} = 0.45$ case.

3.3 Full-cycle test

The final example is dedicated to showing the crack closing and reopening behavior occurring in full-cycle tests. For this purpose, the high-intensity low-cycle fatigue test of Reinhardt [85], conducted on double-edge notched specimens, is chosen. The test setup and finite element mesh of its numerical model are depicted in Fig. 12. As shown in the figure, the length and width of the beam are 250 and 60 mms, respectively. The thickness of the beam is also 50 mms, included in the numerical model by means of the plane stress assumption.

The test is simulated by imposing prescribed opposing displacements on the left and right edges of the specimen. The recorded reaction forces are divided by the cross-section area of the specimen to represent the average stress. The average relative displacement of two vertical lines that are offset by 17.5 mms from the mid-section of the specimen is also recorded to generate the stress–deflection curves.

The contribution of the discontinuity strain field is assessed using four different values of d_{cd} , including 1.00, 0.60, 0.40, and 0.20. The concrete damaged plasticity model of Abaqus is also utilized to simulate the test. The material properties employed in the numerical model are presented in Table 3.

The stress versus deflection responses of the numerical models are plotted on the experimental data in Fig. 13. No sign of stiffness degradation can be observed in the unloading branches of the Abaqus model and the $d_{cd} = 1.00$ case. On the other hand, by decreasing the value of d_{cr} , the contribution of the discontinuity strain field, which reveals itself in the activation of the unilateral effects under less permanent deflection, becomes more pronounced.

4 Conclusion

This paper introduces a new term to the conventional additive strain decomposition to prevent the excessive unrealistic growth of irrecoverable deformations to reproduce the entire failure process of solids.

The issue of excessive growth of irrecoverable deformations is rarely addressed (see for example [86, 87]) since it only manifests itself if the unilateral effects resulting from the closing and reopening of fully formed cracks are of

interest. However, this is the case in the area of low cycle fracture/fatigue as caused by earthquakes in civil engineering structures, for example. We demonstrated the problem arising from the mentioned excessive strains which are inherent to other plastic damage models and showed how these strains cause a faulty stress redistribution upon load reversal.

We called the newly introduced term *discontinuity strain field* since it mimics a discontinuity, yet it is defined at the infinitesimal element level. We demonstrated that introduction of the discontinuity strain field to the conventional additive strain decomposition of the plasticity theory avoids the built up of excessive strains by means of three numerical examples: a pure mode I cracking, a mixed-mode cracking, and a high-intensity low-cycle fatigue test. It is worth mentioning that, although we used the discontinuity strain field to resemble the unilateral effects arising from the collision of the opposing crack faces, it can be used to represent any kind of discontinuity.

Acknowledgements The work was supported by the Alexander von Humboldt Foundation, the Geothermal-Alliance Bavaria (GAB) by the Bavarian State Ministry of Science and the Arts (StMWK) and Deutsche Forschungsgemeinschaft (DFG, Germany) through the project 414265976 TRR 277 C-01.

Funding Open Access funding enabled and organized by Projekt DEAL.

Open Access This article is licensed under a Creative Commons Attribution 4.0 International License, which permits use, sharing, adaptation, distribution and reproduction in any medium or format, as long as you give appropriate credit to the original author(s) and the source, provide a link to the Creative Commons licence, and indicate if changes were made. The images or other third party material in this article are included in the article's Creative Commons licence, unless indicated otherwise in a credit line to the material. If material is not included in the article's Creative Commons licence and your intended use is not permitted by statutory regulation or exceeds the permitted use, you will need to obtain permission directly from the copyright holder. To view a copy of this licence, visit <http://creativecommons.org/licenses/by/4.0/>.

References

1. Cervera M, Barbat G, Chiumenti M, Wu J-Y (2022) A comparative review of XFEM, mixed fem and phase-field models for quasi-brittle cracking. *Arch Comput Methods Eng* 29(2):1009–1083
2. Bui TQ, Tran HT (2022) Dynamic brittle fracture with a new energy limiter-based scalar damage model. *Comput Mech* 69(6):1323–1346
3. Deng S, Apelian D, Bostanabad R (2023) Adaptive spatiotemporal dimension reduction in concurrent multiscale damage analysis. *Comput Mech* 72(1):3–35
4. Daneshyar A, Ghaemian M, Du C (2023) A fracture energy-based viscoelastic–viscoplastic–anisotropic damage model for rate-dependent cracking of concrete. *Int J Fract* 241(1):1–26
5. Hennig P, Kästner M, Maier R, Morgenstern P, Peterseim D (2022). In: Schröder J, Wriggers P (eds) *Adaptive isogeometric phase-field modeling of weak and strong discontinuities*. Springer, Cham, pp 243–282

6. Kalina M, Schneider T, Brummund J, Kästner M (2023) Overview of phase-field models for fatigue fracture in a unified framework. *Eng Fract Mech* 109318
7. Dammaß F, Kalina KA, Ambati M, Kästner M (2022) Phase-field modelling and analysis of rate-dependent fracture phenomena at finite deformation. *Comput Mech*. <https://doi.org/10.1007/s00466-023-02310-1>
8. Löhnert S, Krüger C, Klemp T, Munk L (2023) An enriched phase-field method for the efficient simulation of fracture processes. *Comput Mech* 71(5):1015–1039
9. Haghighat E, Santillán D (2022) An efficient phase-field model of shear fractures using deviatoric stress split. *Comput Mech*. <https://doi.org/10.1007/s00466-023-02348-1>
10. Schapira Y, Radtke L, Kollmannsberger S, Düster A (2023) Performance of acceleration techniques for staggered phase-field solutions. *Comput Methods Appl Mech Eng* 410:116029
11. Pantò B, Macorini L, Izzuddin B (2022) A two-level macroscale continuum description with embedded discontinuities for nonlinear analysis of brick/block masonry. *Comput Mech* 69(3):865–890
12. Bach DP, Brancherie D, Cauvin L (2022) An embedded-fem approach accounting for the size effect in nanocomposites. *Comput Mech* 70(4):745–762
13. Nikolić M (2022) Discrete element model for the failure analysis of partially saturated porous media with propagating cracks represented with embedded strong discontinuities. *Comput Methods Appl Mech Eng* 390:114482
14. Benvenuti E, Orlando N (2021) A mesh-independent framework for crack tracking in elastodamaging materials through the regularized extended finite element method. *Comput Mech* 68(1):25–49
15. Schmidt M, Noël L, Doble K, Evans JA, Maute K (2023) Extended isogeometric analysis of multi-material and multi-physics problems using hierarchical b-splines. *Comput Mech* 71(6):1179–1203
16. Bento MH, Proença SP, Duarte CA (2023) Recovery strategies, a posteriori error estimation, and local error indication for second-order g/xfem and fem. *Int J Numer Methods Eng* 124(13):3025–3062
17. Kachanov LM (1958) On creep rupture time. *Izvestiya Akademii Nauk. SSSR Otdelenie Tekhnicheskikh Nauk. Energetika i Avtomatika* 8:26–31
18. Ladeveze P (1983) On an anisotropic damage theory. *Proc CNRS Int Coll* 351:355–363
19. Leckie F, Onat E (1981) Tensorial nature of damage measuring internal variables. In: *Physical non-linearities in structural analysis: symposium Senlis, France May 27–30, 1980*. Springer, Cham, pp 140–155
20. Chaboche J-L (1984) Anisotropic creep damage in the framework of continuum damage mechanics. *Nucl Eng Des* 79(3):309–319
21. Chow C, Wang J (1987) An anisotropic theory of elasticity for continuum damage mechanics. *Int J Fract* 33:3–16
22. Ladeveze P, Lemaitre J (1984) Damage effective stress in quasi-unilateral conditions. In: *The 16th International congress of theoretical and applied mechanics*, Lyngby, Denmark
23. Desmorat R (2000) Quasi-unilateral conditions in anisotropic elasticity. *CR Acad Sci Paris série IIB* 328:445–450
24. Kuhn C, Müller R (2010) A continuum phase field model for fracture. *Eng Fract Mech* 77(18):3625–3634
25. Schlüter A, Willenbücher A, Kuhn C, Müller R (2014) Phase field approximation of dynamic brittle fracture. *Comput Mech* 54:1141–1161
26. Miehe C, Aldakheel F, Raina A (2016) Phase field modeling of ductile fracture at finite strains: a variational gradient-extended plasticity-damage theory. *Int J Plast* 84:1–32
27. Alessi R, Vidoli S, De Lorenzis L (2018) A phenomenological approach to fatigue with a variational phase-field model: the one-dimensional case. *Eng Fract Mech* 190:53–73
28. Schreiber C, Etrich T, Kuhn C, Müller R (2021) A phase field modeling approach of crack growth in materials with anisotropic fracture toughness. In: *2nd international conference of the DFG international research training group 2057—physical modeling for virtual manufacturing (iPMVM 2020)* Schloss Dagstuhl-Leibniz-Zentrum für Informatik
29. Bazant ZP, Planas J (2019) *Fracture and size effect in concrete and other quasibrittle materials*. Routledge, Oxfordshire
30. Rabczuk T (2013) Computational methods for fracture in brittle and quasi-brittle solids: state-of-the-art review and future perspectives. *Int Sch Res Notices*. <https://doi.org/10.1155/2013/849231>
31. Moës N, Belytschko T (2002) Extended finite element method for cohesive crack growth. *Eng Fract Mech* 69(7):813–833
32. Bocca P, Carpinteri A, Valente S (1991) Mixed mode fracture of concrete. *Int J Solids Struct* 27(9):1139–1153
33. Tvergaard V, Hutchinson JW (1996) Effect of strain-dependent cohesive zone model on predictions of crack growth resistance. *Int J Solids Struct* 33(20–22):3297–3308
34. Camacho GT, Ortiz M (1996) Computational modelling of impact damage in brittle materials. *Int J Solids Struct* 33(20–22):2899–2938
35. Tjssens MG, Sluys BL, Giessen E (2000) Numerical simulation of quasi-brittle fracture using damaging cohesive surfaces. *Eur J Mech A/Solids* 19(5):761–779
36. Bittencourt TN, Llorca J, Ingraffea AR (2003) Simulation of arbitrary, cohesive crack propagation. In: *Fracture mechanics of concrete structures: proceedings of the first international conference on fracture mechanics of concrete structures (FraMCoS1)*, held at Beaver Run Resort, Breckenridge, Colorado, USA, 1–5 June 1992, vol 1. CRC Press, p 339
37. Turon A, Davila CG, Camanho PP, Costa J (2007) An engineering solution for mesh size effects in the simulation of delamination using cohesive zone models. *Eng Fract Mech* 74(10):1665–1682
38. Campilho RD, Banea MD, Neto J, Silva LF (2013) Modelling adhesive joints with cohesive zone models: effect of the cohesive law shape of the adhesive layer. *Int J Adhes Adhes* 44:48–56
39. Töller F, Löhnert S, Wriggers P (2019) Bulk material models in cohesive zone elements for simulation of joining zones. *Finite Elem Anal Des* 164:42–54
40. Yang T, Liechti KM, Huang R (2020) A multiscale cohesive zone model for rate-dependent fracture of interfaces. *J Mech Phys Solids* 145:104142
41. Töller F, Löhnert S, Wriggers P (2020) Applying membrane mode enhanced cohesive zone elements on tailored forming components. *Metals* 10(10):1333
42. Belytschko T, Black T (1999) Elastic crack growth in finite elements with minimal remeshing. *Int J Numer Methods Eng* 45(5):601–620
43. Moës N, Dolbow J, Belytschko T (1999) A finite element method for crack growth without remeshing. *Int J Numer Methods Eng* 46(1):131–150
44. Wells GN, Sluys L (2001) A new method for modelling cohesive cracks using finite elements. *Int J Numer Methods Eng* 50(12):2667–2682
45. Stolarska M, Chopp DL, Moës N, Belytschko T (2001) Modelling crack growth by level sets in the extended finite element method. *Int J Numer Methods Eng* 51(8):943–960
46. Asferg JL, Poulsen PN, Nielsen LO (2007) A consistent partly cracked XFEM element for cohesive crack growth. *Int J Numer Methods Eng* 72(4):464–485
47. Unger JF, Eckardt S, Könke C (2007) Modelling of cohesive crack growth in concrete structures with the extended finite element method. *Comput Methods Appl Mech Eng* 196(41–44):4087–4100
48. Zhang X, Bui TQ (2015) A fictitious crack XFEM with two new solution algorithms for cohesive crack growth modeling in concrete structures. *Eng Comput* 32(2):473–497

49. Kästner M, Müller S, Ulbricht V (2013) Xfem modelling of inelastic material behaviour and interface failure in textile-reinforced composites. *Procedia Mater. Sci.* 2:43–51
50. Daneshyar A, Mohammadi S (2013) Strong tangential discontinuity modeling of shear bands using the extended finite element method. *Comput Mech* 52:1023–1038
51. Pike MG, Oskay C (2015) XFEM modeling of short microfiber reinforced composites with cohesive interfaces. *Finite Elem Anal Des* 106:16–31
52. Kästner M, Müller S, Hirsch F, Pap J-S, Jansen I, Ulbricht V (2016) XFEM modeling of interface failure in adhesively bonded fiber-reinforced polymers. *Adv Eng Mater* 18(3):417–42
53. Idkaidek A, Koric S, Jasiuk I (2018) Fracture analysis of multi-osteons cortical bone using XFEM. *Comput Mech* 62:171–184
54. Simone A, Wells GN, Sluys LJ (2003) From continuous to discontinuous failure in a gradient-enhanced continuum damage model. *Comput Methods Appl Mech Eng* 192(41–42):4581–4607
55. Moës N, Stolz C, Bernard P-E, Chevaugeon N (2011) A level set based model for damage growth: the thick level set approach. *Int J Numer Methods Eng* 86(3):358–380
56. Han J, Shintaku Y, Moriguchi S, Terada K (2023) A transition scheme from diffusive to discrete crack topologies at finite strain during the course of a staggered iterative procedure. *Int J Numer Methods Eng* 124(6):1405–1433
57. Sun J, Löhner S (2021) 3d thermo-mechanical dynamic crack propagation with the XFEM and gradient enhanced damage. *PAMM* 20(1):202000271
58. Pandey V, Singh I, Mishra B (2023) A new creep-fatigue interaction damage model and CDM-XFEM framework for creep-fatigue crack growth simulations. *Theor Appl Fract Mech* 124:103740
59. Puccia M, Spada A, Giambanco G (2023) Finite elements with embedded interphases for strain localization in quasi-brittle materials. *Eng Fract Mech* 277:108956
60. Seabra MR, Šuštarčič P, Sa JM, Rodič T (2013) Damage driven crack initiation and propagation in ductile metals using XFEM. *Comput Mech* 52:161–179
61. Sarkar S, Singh IV, Mishra B (2021) A simplified continuous-discontinuous approach to fracture based on decoupled localizing gradient damage method. *Comput Methods Appl Mech Eng* 383:113893
62. Negi A, Kumar S (2022) A continuous-discontinuous localizing gradient damage framework for failure analysis of quasi-brittle materials. *Comput Methods Appl Mech Eng* 390:114434
63. Cu villiez S, Feyel F, Lorentz E, Michel-Ponnelle S (2012) A finite element approach coupling a continuous gradient damage model and a cohesive zone model within the framework of quasi-brittle failure. *Comput Methods Appl Mech Eng* 237:244–259
64. Roth S-N, Léger P, Soulaïmani A (2015) A combined XFEM-damage mechanics approach for concrete crack propagation. *Comput Methods Appl Mech Eng* 283:923–955
65. Wang Y, Waisman H (2016) From diffuse damage to sharp cohesive cracks: a coupled XFEM framework for failure analysis of quasi-brittle materials. *Comput Methods Appl Mech Eng* 299:57–89
66. Cervera M, Wu J-Y (2015) On the conformity of strong, regularized, embedded and smeared discontinuity approaches for the modeling of localized failure in solids. *Int J Solids Struct* 71:19–38
67. Hartmann S, Kamlah M, Koch A (1998) Numerical aspects of a non-proportional cyclic plasticity model under plane stress conditions. *Int J Numer Methods Eng* 42(8):1477–1498
68. Cervera M, Tesei C, Ventura G (2018) Cracking of quasi-brittle structures under monotonic and cyclic loadings: a $d+/d-$ damage model with stiffness recovery in shear. *Int J Solids Struct* 135:148–171
69. Alaimo G, Carraturo M, Korshunova N, Kollmannsberger S (2021) Numerical evaluation of high cycle fatigue life for additively manufactured stainless steel 316L lattice structures: preliminary considerations. *Mater Design Process Commun* 3(4):249
70. Zhang J, Liu W, Zhu Q, Shao J (2023) A novel elastic-plastic damage model for rock materials considering micro-structural degradation due to cyclic fatigue. *Int J Plast* 160:103496
71. Wächter M, Leicher M, Hupka M, Leistner C, Masendorf L, Treutler K, Kamper S, Esderts A, Wesling V, Hartmann S (2020) Monotonic and fatigue properties of steel material manufactured by wire arc additive manufacturing. *Appl Sci* 10(15):5238
72. Oneschkow N, Timmermann T, Löhner S (2022) Compressive fatigue behaviour of high-strength concrete and mortar: experimental investigations and computational modelling. *Materials* 15(1):319
73. Schröder J, Pise M, Brands D, Gebuhr G, Anders S (2022) Phase-field modeling of fracture in high performance concrete during low-cycle fatigue: numerical calibration and experimental validation. *Comput Methods Appl Mech Eng* 398:115181
74. Pise M, Brands D, Schröder J, Gebuhr G, Anders S (2023) Phenomenological material model for damage in steel-fiber reinforced high performance concrete during low cycle fatigue. *PAMM* 22(1):202200236
75. Daneshyar A, Sotoudeh P (2021) Ghaemian M (2021) Wave propagation in a three-dimensional half-space with semi-infinite irregularities. *Waves Random Complex Media* 10(1080/17455030):1974602
76. Coronelli D, Muttoni A, Martinelli L, Del Vecchio C, d’Aragona MG, Lignola GP, Prota A, Kagermanov A, Marinković M (2023) Flat slab response for seismic and cyclic actions prediction with numerical models. *Eng Struct* 289:116307
77. Schiavoni M, Giordano E, Roscini F, Clementi F (2023) Advanced numerical insights for an effective seismic assessment of historical masonry aggregates. *Eng Struct* 285:115997
78. Feenstra PH, De Borst R (1995) A plasticity model and algorithm for mode-I cracking in concrete. *Int J Numer Methods Eng* 38(15):2509–2529
79. Souza Neto EA, Peric D, Owen DR (2011) Computational methods for plasticity: theory and applications. Wiley, Hoboken
80. Ortiz M (1985) A constitutive theory for the inelastic behavior of concrete. *Mech Mater* 4(1):67–93
81. Daneshyar A, Ghaemian M (2020) Fe^2 investigation of aggregate characteristics effect on fracture properties of concrete. *Int J Fract* 226(2):243–261
82. Grassl P, Jirásek M (2006) Plastic model with non-local damage applied to concrete. *Int J Numer Anal Meth Geomech* 30(1):71–90
83. Daneshyar A, Sotoudeh P, Ghaemian M (2023) The scaled boundary finite element method for dispersive wave propagation in higher-order continua. *Int J Numer Methods Eng* 124(4):880–927
84. Perdikaris PC, Romeo A (1995) Size effect on fracture energy of concrete and stability issues in three-point bending fracture toughness testing. *Mater J* 92(5):483–496
85. Reinhardt HW (1984) Fracture mechanics of an elastic softening material like concrete. *HERON* 29(2):1984
86. Lee J, Fenves GL (1998) A plastic-damage concrete model for earthquake analysis of dams. *Earthq Eng Struct Dyn* 27(9):937–956
87. Omid O, Lotfi V (2013) Continuum large cracking in a rate-dependent plastic-damage model for cyclic-loaded concrete structures. *Int J Numer Anal Methods Geomech* 37(10):1363–1390